

Ultra-High In-Device Electro-Optic Coefficient of $r_{33} = 390$ pm/V Demonstrated in a Silicon-Organic Hybrid (SOH) Modulator

CLEMENS KIENINGER,^{1,2,*} YASAR KUTUVANTAVIDA,^{1,2} DELWIN L. ELDER,³ STEFAN WOLF,¹ HEINER ZWICKEL,¹ MATTHIAS BLAICHER,¹ JUNED N. KEMAL,¹ MATTHIAS LAUERMANN,⁴ SEBASTIAN RANDEL,¹ WOLFGANG FREUDE,¹ LARRY R. DALTON,³ AND CHRISTIAN KOOS^{1,2,*}

¹Karlsruhe Institute of Technology (KIT), Institute of Photonics and Quantum Electronics (IPQ), Karlsruhe 76131, Germany

²Karlsruhe Institute of Technology (KIT), Institute of Microstructure Technology (IMT), Karlsruhe 76344, Germany

³University of Washington, Department of Chemistry, Seattle, WA 98195, USA

⁴Now with: Infinera Corporation, Sunnyvale, CA 94089, USA

*Corresponding authors: clemens.kieninger@kit.edu, christian.koos@kit.edu

Efficient electro-optic (EO) modulators crucially rely on advanced materials that exhibit strong electro-optic activity and that can be integrated into high-speed phase shifter structures. In this paper, we demonstrate record-high in-device EO coefficients of up to $r_{33} = 390$ pm/V achieved in a silicon-organic hybrid (SOH) Mach-Zehnder Modulator (MZM) using the EO chromophore JRD1. This is the highest material-related in-device EO coefficient hitherto achieved in a Pockels-type modulator at any operating wavelength. The π -voltage of the 1.5 mm-long device amounts to 210 mV, leading to a voltage-length product of $U_{\pi}L = 320$ V μ m – the lowest value reported for MZM based on low-loss dielectric waveguides. The viability of the devices is demonstrated by generating error-free on-off-keying (OOK) signals at 40 Gbit/s at a drive voltage as low as 140 mV_{pp}. We expect that efficient high-speed EO modulators will not only have major impact in the field of optical communications, but will also open new avenues towards ultra-fast photonic-electronic signal processing.

OCIS codes: (160.2100) Electro-optical materials ; (230.2090) Electro-optical devices; (250.4110) Modulators; (130.3120) Integrated optics devices; (200.4650) Optical interconnects, (250.5300) Photonic integrated circuits.

Electro-optic (EO) phase modulators are key for many applications such as optical communications [1], optical signal processing [2], or high-precision metrology [3]. Among the various concepts, devices based on the linear electro-optic effect (Pockels effect) are particularly powerful, providing pure phase modulation at high speed, thereby enabling the generation of high-quality optical data signals based on advanced modulation formats [4–6]. Pockels-effect modulators can be broadly subdivided in two categories: The first one comprises conventional devices, where optical waveguides are directly fabricated in crystalline or amorphous EO materials. This approach is used for, e.g., LiNbO₃ devices [7], all-polymer modulators [8], or devices based on III-V compound semiconductors [9,10], which often exploit a combination of the Pockels effect and other phase modulation mechanisms such as the quantum confined stark effect (QCSE) or the Franz Keldysh effect. More recently, a second category of devices has emerged, relying on hybrid integration approaches that combine

Pockels-type EO materials with dielectric or plasmonic waveguide structures that do not feature any EO activity. This approach is often used to overcome the intrinsic lack of second-order nonlinearities in otherwise highly attractive material systems such as the silicon photonics platform. Examples of this category comprise the concepts of silicon-organic hybrid (SOH) [11–13] and plasmonic-organic hybrid (POH) [14–16] devices, that combine organic EO (OEO) materials with silicon photonic or plasmonic waveguide structures or other approaches that exploit hybrid combinations of lithium-niobate (LiNbO₃) thin films [17] or barium-titanate (BaTiO₃) layers [18] with silicon-on-insulator (SOI) waveguides.

In all of these cases, one of the most important design goals is to achieve high modulation efficiency, i.e., large phase shifts for low operating voltages and small device lengths, along with low optical insertion loss. For Mach-Zehnder modulators (MZM), the modulation efficiency can be quantified by the product $U_{\pi}L$ of the phase shifter

length L and the voltage U_n that is required to achieve a phase shift of π between the optical signals at the output of the MZM arms [13]. For Pockels-effect modulators based on dielectric waveguides, the lowest demonstrated $U_n L$ -product amounts to 0.5 Vmm, achieved in an SOH device that combines a silicon photonic slot waveguide with the OEO chromophore DLD164 [19]. For plasmonic waveguides, even lower values down to $U_n L = 0.05$ Vmm can be achieved [20]. However, while these devices feature large electro-optic bandwidths [21], they suffer from intrinsic propagation losses, which limit the range of practical device lengths to a few tens of micrometers [13,20]. This effect can be quantified by the product $aU_n L$ which combines the π -voltage U_n , the phase shifter length L , and the waveguide propagation loss a measured in dB/mm. Previously demonstrated values of $aU_n L$ amount to 2.8 VdB for SOH devices [19], indicating that a phase shifter with an insertion loss of 1 dB requires an operating voltage of 2.8 V. For the previously mentioned POH devices [20], this number amounts to 25 VdB.

All these figures of merit can be improved by using a Pockels-type material with strong EO activity, quantified by the EO coefficient r . In this context, it is important to note that the EO coefficient achieved in actual devices may be significantly smaller than the EO coefficient of the corresponding bulk material. As an example, while high-performance EO crystals such as BaTiO₃ may feature bulk EO coefficients in excess of $r_{42} = 1000$ pm/V [22], the highest in-device EO coefficients demonstrated so far amount to $r_{33} = 220$ pm/V ($r_{33} = 325$ pm/V) for a wavelength of 1.55 μm (1.25 μm), achieved for an organic binary-chromophore compound in a POH modulator [23].

Here we demonstrate a record-high in-device electro-optic coefficient of $r_{33} = 390$ pm/V, measured at a wavelength of 1.55 μm in an SOH modulator that uses the organic EO material JRD1 [24] as a cladding. To the best of our knowledge, this is the highest in-device EO coefficient ever achieved in a Pockels-type modulator at any operating wavelength. The devices feature $U_n L$ -products down to 0.32 Vmm – the lowest value ever achieved for a modulator based on low-loss dielectric waveguides. We measure a $aU_n L$ -product of 1.2 VdB, which is on par with the lowest values reported so far [10]. The viability of the device is demonstrated by generation of error-free on-off-keying (OOK) signals at a data rate of 40 Gbit/s at peak-to-peak operation voltages of only $U_{pp} = 140$ mV_{pp}. This is the lowest value ever demonstrated for error-free signal generation at practically relevant data rates.

SOH modulator concept and material design

The concept of an SOH phase shifter is depicted in Fig. 1(a). The device comprises a silicon (Si) slot waveguide formed by two 240 nm wide and 220 nm high Si rails that are separated by a narrow slot, which is filled by the OEO material. An electrical connection between the Si rails and the aluminum (Al) transmission lines is achieved by 70 nm high doped Si slabs and Al vias. Both optical and RF field are tightly confined in the slot region, leading to a strong modal overlap in the OEO material and hence to highly efficient phase modulation. The waveguide structures are fabricated on standard silicon-on-insulator (SOI) wafers in a commercial silicon photonic foundry process using standard 248 nm deep-UV (DUV) lithography. As an OEO cladding, we use the neat chromophore material JRD1 [24], which is locally deposited on the slot waveguides in a dedicated post-processing step. The molecular structure of JRD1 is displayed in Fig. 1(b). The material is the result of theory-guided optimization of the previously used OEO chromophore YLD124 [25]. Both materials share common donor and acceptor groups that are separated by a π -conjugated bridge. Due to this common chromophore core, both materials show a very similar molecular hyperpolarizability [26]. However, JRD1 features bulky phenyl side groups denoted as R1 in Fig. 1(b), rather than methyl

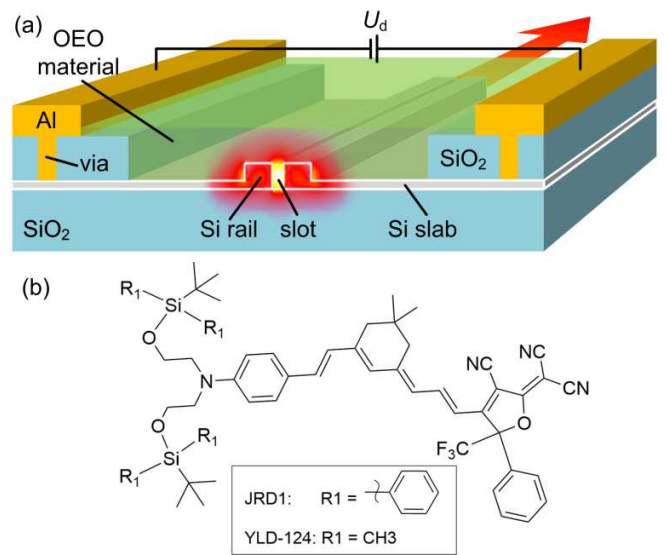


Fig. 1 Concept of a silicon-organic hybrid (SOH) phase shifter. (a) Device principle. The phase shifter comprises a Si slot waveguide formed by a pair of Si rails. The slot is filled with an organic electro-optic (OEO) material. The rails are electrically connected to an aluminum (Al) transmission line via doped Si slabs and Al vias, such that an externally applied voltage U_d drops entirely across the narrow slot. At the same time, the optical mode is tightly confined to the OEO material in the slot, resulting in highly efficient phase modulation. (b) Molecular structure of the employed OEO material JRD1 and of the previously used [25] material YLD124. Compared to YLD124, JRD1 features bulky phenyl side groups denoted as R1, which decrease inter-molecular interactions and thus increase molecular mobility during electric-field poling. This is instrumental for achieving record-high in-device EO coefficients.

groups as used in YLD124. The bulkier side groups significantly increase the intermolecular distance of neighboring chromophores, which reduces the strength of detrimental dipole-dipole interactions that promote centrosymmetric pairing of chromophores [27]. As a result, JRD1 chromophores can be used in high number densities without a polymer host [27], while still maintaining high molecular mobility during electric-field poling and avoiding unwanted centrosymmetric pairing of chromophores. This leads to large EO coefficients of up to $r_{33} = 550$ pm/V in bulk samples of JRD1 [24] – more than a 2-fold increase of r_{33} as compared to YLD124 [24]. Note that the glass transition temperatures of JRD1 ($T_g = 82^\circ\text{C}$) and YLD124 ($T_g = 81^\circ\text{C}$) are comparable [28]. Generally, due to the relatively low T_g , the materials are currently still prone to thermally induced relaxation of chromophore orientation when operated at elevated temperatures. Increased thermal stability without considerably impairing the EO activity is expected when JRD1 is synthetically modified with crosslinking agents which enable post-poling lattice hardening. This approach has led to similar classes of OEO materials with a T_g of up to 250°C [29].

Device preparation and characterization

For our experimental demonstration, we use Mach-Zehnder type SOH modulators rather than the phase modulator shown in Fig. 1(a). The concept of an SOH Mach-Zehnder modulator (MZM) is schematically depicted in Fig. 2(a). The coplanar transmission line is realized in a ground-signal-ground (GSG) configuration. Light is coupled to and from the chip via grating couplers (GC), and a multi-mode interference coupler (MMI) is used to split and combine the light of the two arms

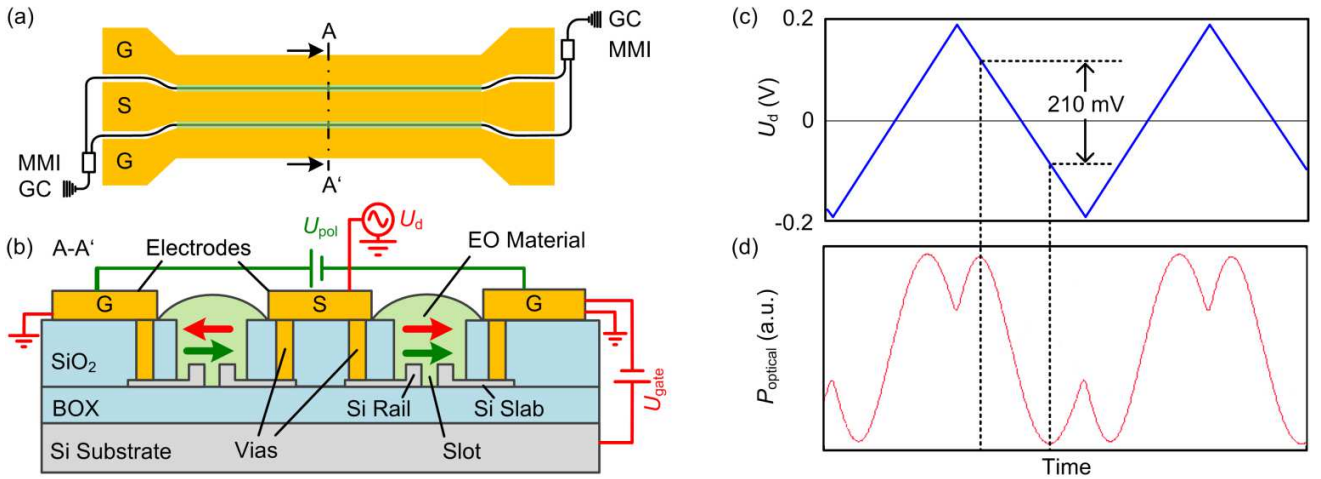


Fig. 2 Schematic of an SOH MZM and measurement of U_π . **(a)** Top view. Light is coupled to and from the device via grating couplers (GC). The coplanar transmission line is arranged in a ground-signal-ground (GSG) configuration. A pair of multi-mode interference (MMI) couplers is used to split and recombine the light of the two MZM arms. **(b)** Cross section of the two arms of the SOH MZM at the position defined by the dash-dotted line A-A' in (a). Each arm comprises an SOH phase shifter. A one-time poling process is required to achieve a macroscopic in-device r_{33} after deposition of the EO chromophores from solution. To this end, a poling voltage U_{pol} is applied across the floating ground electrodes at elevated temperature close to $T_g = 82^\circ\text{C}$, thereby inducing an electric poling field (green arrows) in the slot regions. The dipoles of the EO material align along the poling field in acentric order. After cooling the device down to room temperature, U_{pol} is removed and the acentric order of the chromophores is conserved. For modulation, a radio-frequency (RF) signal voltage U_d induces electric fields in the slots (red arrows) that are antiparallel (parallel) to the aligned chromophores in the left (right) arm of the MZM, thereby realizing push-pull operation. The bandwidth of the modulator can be increased by decreasing the resistance of the silicon slab. This is achieved by applying a gate voltage U_{gate} between the silicon substrate and the ground electrodes. **(c)** Low-speed triangular drive signal for the static U_π measurement as a function of time. **(d)** Over-modulated optical signal as a function of time when the modulator is fed by the waveform depicted in (c). The MZM is biased in its quadrature point and the π -voltage U_π can be directly read from the voltage increment needed to drive the device from minimum to maximum transmission. For the depicted measurements, we extract a π -voltage of 210 mV, corresponding to a π -voltage-length product of $U_\pi L = 0.32$ Vmm.

of the MZM. Fig. 2(b) shows a cross-section of the two MZM arms at the position indicated by the dash-dotted line A-A' in Fig. 2(a). Each MZM arm comprises an SOH phase shifter with a JRD1 cladding. The material is deposited in solution, thus the EO chromophores are randomly oriented after deposition. An average acentric orientation and thus a macroscopic EO effect is obtained by a one-time electric-field poling process [30]. To this end, the chip is heated close to the glass transition temperature of JRD1 ($T_g = 82^\circ\text{C}$), and a DC poling voltage U_{pol} is then applied across the floating ground electrodes, inducing an electric poling field E_{pol} (green arrows) in the EO material which aligns the dipolar chromophores. This order is frozen by cooling the device to room temperature while maintaining the poling field. The device enables simple push-pull-operation: An RF voltage applied to the GSG transmission line of the MZM induces electric fields in the slots (red arrows) that are parallel to the orientation of the EO chromophores (green arrows) in the right arm and antiparallel in the left arm of the MZM. In order to increase the bandwidth of the device, the resistivity of the doped silicon slabs can be decreased by generating an electron accumulation layer [31]. In the experiment, this is realized by applying a gate voltage U_{gate} between the Si substrate and the ground electrode.

To quantify the modulation efficiency, we measure the static π -voltage of the device, see Supplement 1 for details on the experimental setup. A low-frequency triangular waveform obtained from a function generator (FG) is applied to the signal electrode of the SOH MZM, which is fed by an optical CW signal at a wavelength of 1550 nm through an on-chip grating coupler. The modulated optical signal is detected by a low-speed photo-diode (PD). Both, the output of the FG (blue curve) and the output of the PD (red curve) are recorded simultaneously by an oscilloscope, see Fig. 2(c) and (d). The modulator

is biased in its quadrature point, and the peak-to-peak drive voltage amplitude is chosen larger than the π -voltage such that the MZM is over-modulated. The π -voltage then corresponds to the voltage difference needed to drive the MZM from its minimum to its maximum transmission point.

For achieving high electro-optic activity, one of the essential parameters is the applied electric poling field E_{pol} . In our experiments, we systematically varied this parameter and measured the resulting $U_\pi L$ -product for two different sets of devices having slot widths of 190 nm and 150 nm. The experimental results are summarized in Fig. 3(a), where red crosses (blue circles) correspond to slot widths of 190 nm (150 nm). For both sets of devices, the measured $U_\pi L$ -products first decrease with increasing E_{pol} , then level off, and finally rise again. The rise is attributed to the onset of conductance, possibly in combination with dielectric breakdown. This can inflict permanent damage of the material, which is found by attempting to re-pole the two devices indicated by the red ellipse. In the re-poling experiment, we use moderate poling fields of $200\text{ V}/\mu\text{m}$, leading to measured $U_\pi L$ -products of 3.5 Vmm and 4.0 Vmm. This is much worse than the values of approximately 1.7 Vmm that are typically achieved for this poling field. For both sets of devices, the lowest measured $U_\pi L$ -product amounts to 0.32 Vmm, which was achieved at poling fields of $390\text{ V}/\mu\text{m}$ ($455\text{ V}/\mu\text{m}$) for the 190 nm (150 nm) slots. To the best of our knowledge this is the lowest value of $U_\pi L$ hitherto demonstrated for a non-resonant device based on low-loss dielectric waveguides. The propagation loss of the phase-shifter section amounts to about 3.9 dB/mm, see Supplement 1, leading to an $aU_\pi L$ value of 1.2 VdB. This is on par with ultra-low $aU_\pi L$ values of 1.3 VdB achieved for advanced InP-based phase modulators, which combine a rather large $U_\pi L$ -product of 5.4 Vmm with a very low on-chip propagation loss of

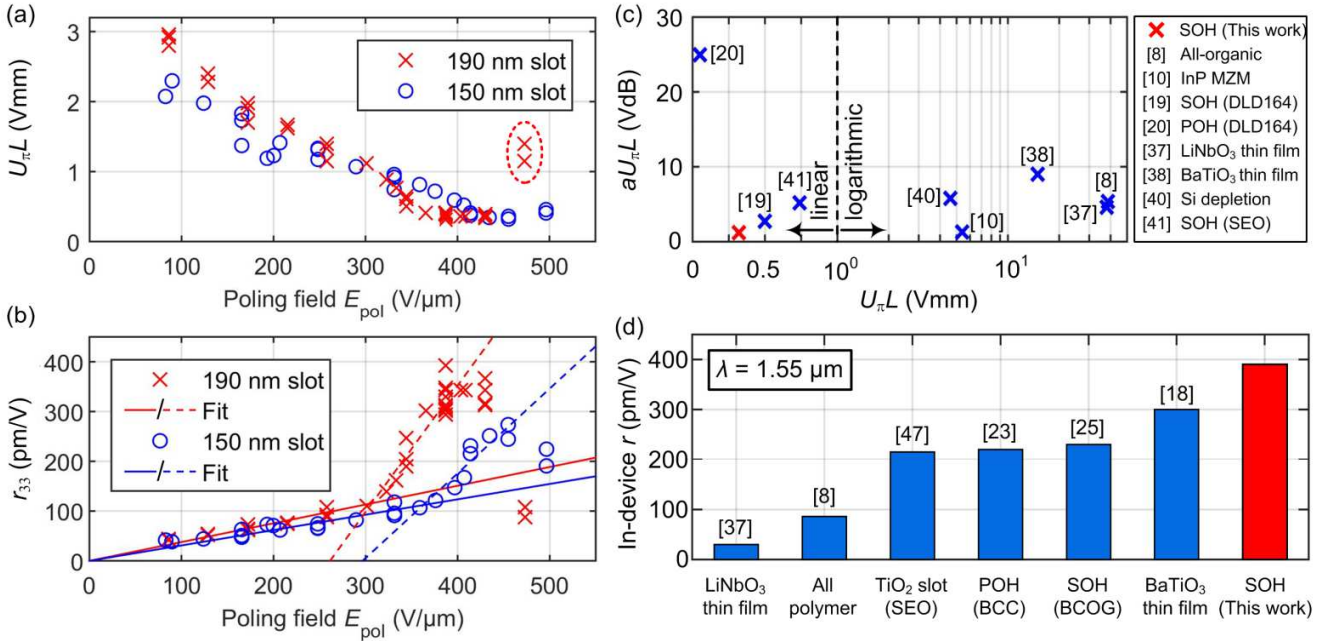


Fig. 3 Electro-optic characterization and benchmarking of the SOH MZM. **(a)** Measured $U_{\pi}L$ -products as a function of the poling field E_{pol} . Two sets of devices are investigated: Red crosses correspond to samples with slot widths of 190 nm, and blue circles indicate slot widths of 150 nm. The $U_{\pi}L$ -products decrease for an increasing poling field, level off, and rise again. The rise is attributed to the onset of conductance, possibly in combination with dielectric breakdown, which may cause permanent damage of the affected chromophores. This is confirmed by the fact that the samples indicated by the large red ellipse do not recover typical EO activity when re-poling at moderate fields of 200 V/ μ m is attempted. The minimum $U_{\pi}L$ product amounts to 0.32 Vmm for both sample geometries. **(b)** Calculated r_{33} as a function of E_{pol} . Red crosses (blue circles) indicate samples with slot widths of 190 nm (150 nm). For both data sets, r_{33} increases linearly with the poling fields and features a steep increase in slope once a certain threshold poling field is exceeded. The behavior below (above) the threshold poling field is visualized by the red and blue solid (dashed) lines obtained from least square fits to linear functions. The drop of r_{33} at even higher poling fields is attributed to the onset of conductance in the OEO material, possibly in combination with dielectric breakdown. The threshold effect may be explained by surface-chromophore interactions leading to alignment of chromophores along the slot sidewalls – this aspect is subject to theoretical investigations. The maximum r_{33} amounts to 390 pm/V and is obtained for a slot width of 190 nm. Devices with 150 nm wide slots feature systematically lower values of r_{33} , which is attributed to a stronger influence of surface effects in narrower slots. **(c)** Measured $aU_{\pi}L$ -products as a function of the $U_{\pi}L$ -product for various modulator concepts. The abscissa exhibits a linear scale for $U_{\pi}L < 1$ Vmm and a logarithmic scale for $U_{\pi}L \geq 1$ Vmm. Indicated by the proximity to the origin of the figure, SOH MZM combine low voltage-length products with low losses, and hence compare favorably with competing modulator concepts. The device presented in this work shows a $U_{\pi}L$ of 0.32 Vmm and an $aU_{\pi}L$ of 1.2 VdB. Only POH modulators offer a lower $U_{\pi}L$ -product of 0.05 Vmm, which comes, however, at the price of an increased $aU_{\pi}L$ -product of 25 VdB. **(d)** Summary of in-device electro-optic (EO) coefficients r of competing material platforms for integrated EO modulators. For all depicted devices except the BaTiO₃ modulator, the coefficient r refers to the r_{33} element of the corresponding EO tensor. For the BaTiO₃ device an effective EO coefficient which neglects the tensor nature is given since individual tensor components could not be measured. All values given in (d) refer to an operating wavelength of 1550 nm.

2.4 dB/cm [10].

Using the refractive index of JRD1, $n_{EO} = 1.81$ and the simulated fields of the optical and the radio frequency (RF) mode of the device, the measured $U_{\pi}L$ -products in Fig. 3(a) can be linked to the in-device EO coefficient r_{33} , see Supplement 1 for a derivation of the corresponding mathematical relations. The results are shown in Fig. 3(b), where the calculated r_{33} is plotted versus the applied poling field. The red crosses and blue circles correspond again to devices having slot widths of 190 nm and 150 nm, respectively. Remarkably, when increasing the poling field, r_{33} does not exhibit a linear increase with a single slope, as typically observed, e.g., in [32]. Instead, both data sets show a steep increase in slope once a certain threshold poling field is exceeded. To illustrate the two distinctively different poling regimes, we fit a linear function to the measured r_{33} values below (solid line) and above (dashed line) the threshold poling field. At very high poling fields, we observe a roll-off and finally a drop of r_{33} , which is attributed to the onset of conductance, possibly in combination with dielectric breakdown. These data points are omitted for the linear fit. The

unusual dependency of r_{33} on E_{pol} is still under investigation. It may be explained by chromophore interactions at surfaces - recent simulations have shown that chromophores at the sidewalls of POH slot waveguides align in parallel to these sidewalls and do not contribute to the EO activity [20]. As a consequence, poling is only effective at a sufficient distance from the surface, i.e., in the center of the slot region, where the chromophores are initially randomly oriented and become aligned during poling. Most likely, similar effects are present in SOH slot waveguides. It is conceivable that for sufficiently large poling fields, a threshold is reached that triggers the reorientation of chromophores at the sidewalls, leading to a steeper slope of r_{33} . For a better understanding of the underlying mechanisms, further investigations are required and will be subject to a joint theoretical and experimental effort in the near future. To the best of our knowledge the effect has never been reported so far. We attribute this to the fact that in typical sample geometries the maximum applicable poling field is restricted to 100-200 V/ μ m before dielectric breakdown occurs [29,33,34]. This is well below the threshold poling field

observed in our study. The outstanding stability against dielectric breakdown in SOH devices was already observed in previous experiments where fields above $300 \text{ V}/\mu\text{m}$ could be applied without dielectric breakdown [25]. This was attributed to the low number of defects in the EO material filling the nano-scale slot. The maximum calculated r_{33} is achieved for a sample with slot width of 190 nm and amounts to $390 \text{ pm}/\text{V}$. This is the highest material-related in-device EO coefficient ever demonstrated for any material platform and operating wavelength. Devices with slot widths of 150 nm show systematically smaller values of r_{33} . The largest value achieved amounts to only $270 \text{ pm}/\text{V}$. We attribute this to an even higher fraction of chromophores near the surface than in the center of the slot which limits the EO activity. Despite the reduced r_{33} , the MZM with 150 nm slots exhibit the same value for $U_{\pi}L$ as the devices with 190 nm slots, see Fig. 3(a). This non-intuitive finding can be explained by the fact that devices with narrow slot width exhibit a larger overlap of the optical and RF mode, a fact which results in a more efficient modulation that compensates the reduced r_{33} . Note that the threshold effect is less visible in the measurement of the $U_{\pi}L$ -product in Fig. 3(a) due to the inverse relation of r_{33} and $U_{\pi}L$.

For a benchmarking of the presented performance parameters of the SOH MZM, we plot the loss-efficiency product $aU_{\pi}L$ as a function of the voltage-length product $U_{\pi}L$ for competing state-of-the-art EO modulators, which are based on various concepts and technologies. The results are shown in Fig. 3(c) for an operating wavelength of $1.55 \mu\text{m}$, unless stated otherwise. Note that the abscissa features a linear scale for $U_{\pi}L < 1 \text{ Vmm}$ and a logarithmic scale for $U_{\pi}L \geq 1 \text{ Vmm}$. Ideal devices combine low values of $U_{\pi}L$ with low losses and hence low $aU_{\pi}L$ -products, to be found in the lower left-hand corner of the plot, close to the origin. Besides Pockels-effect modulators, the comparison in Fig. 3(c) also includes selected high-speed InP and silicon-based depletion-type devices. In the future, this group might be complemented by highly efficient accumulation-type devices [35,36], which are currently still subject to limited EO modulation bandwidth of a few gigahertz.

The comparison in Fig. 3(c) shows that modulators fabricated on the thin-film LiNbO_3 platform [37] as well as all-organic modulators [8] feature comparatively high $U_{\pi}L$ -products in excess of 38 Vmm , but show also low propagation losses. Hence, despite their large footprint, these devices exhibit moderate $aU_{\pi}L$ -products of around 5 VdB . For the novel BaTiO_3 -on-Si platform, MZM with lower $U_{\pi}L$ -product of 15 Vmm have been demonstrated [38]. While previous device generations suffered from pronounced propagation losses in excess of 4.5 dB/mm , passive waveguides with losses of only 0.6 dB/mm were demonstrated recently [39], potentially leading to loss-efficiency products of $aU_{\pi}L = 9 \text{ VdB}$. State-of-the-art depletion-type Si MZM with U-shaped pn junctions operated at 1310 nm show more efficient modulation with $U_{\pi}L$ -products of 4.6 Vmm and reduced $aU_{\pi}L$ -products down to 5.8 VdB [40]. Similar modulation efficiencies of $U_{\pi}L = 5.4 \text{ Vmm}$ are achieved in indium phosphide (InP) based MZM [10]. At the same time, these devices show significantly reduced propagation losses as compared to silicon-based depletion-type modulators, leading to very low $aU_{\pi}L$ values of only 1.3 VdB . SOH MZM stand out due to their low $U_{\pi}L$ -products of 0.74 Vmm [41] and 0.5 Vmm [19], obtained by the commercial OEO material SEO100 and by the even more efficient neat chromophore DLD164, respectively. However, the propagation loss of SOH slot waveguides is also higher than the losses of advanced InP waveguides, leading to $aU_{\pi}L$ -products of 5 VdB and 2.8 VdB for the two EO materials. The SOH modulators presented in this work outperform these devices by exhibiting $U_{\pi}L$ -products as low as 0.32 Vmm and a propagation loss of about 3.9 dB/mm , which results in a $aU_{\pi}L$ -product of 1.2 VdB . This is on par with the $aU_{\pi}L$ -product of advanced InP modulators, which feature significantly higher $U_{\pi}L$ -products. The $U_{\pi}L$ -

products of POH are even smaller than those of SOH devices, with published values down to 0.05 Vmm [20] when the OEO material DLD164 is employed. However, the small $U_{\pi}L$ -products come at the price of increased propagation losses in the plasmonic slot waveguides, which is reflected in the increased loss-efficiency product of typically $aU_{\pi}L = 25 \text{ VdB}$. Hence, in comparison to all other devices, the SOH modulator presented in this work comes closest to the origin, indicating an ideal combination of high modulation efficiency and low propagation loss of the dielectric waveguide structure. We hence expect that the SOH concept will have major impact on future implementations of optical communication systems and may also open new opportunities in ultra-fast photonic-electronic signal processing, where highly efficient low-loss devices can, e.g., enable advanced electro-optic sampling. SOH devices have previously been demonstrated to enable high-speed coherent [42,43] and non-coherent [44,45] transmission with single-polarization line rates of up to 400 Gbit/s (100 GBd 16QAM) [5].

In Fig. 3(d) we summarize the in-device EO coefficients r achieved in state-of-the-art Pockels-effect EO modulators. For all depicted devices except the BaTiO_3 modulator, the coefficient r refers to the r_{33} element of the corresponding EO tensor. For the BaTiO_3 device, the tensor components could not be measured individually due to the poly-domain structure of the thin film. Instead, r was estimated as an effective EO coefficient by neglecting the tensor nature [18]. Note that the in-device EO coefficients r depicted in Fig. 3(d) are purely material-related and do not comprise additional enhancements that can, e.g., be achieved through slow-light structures [46]. For a better comparison between different EO materials, we examine only the values obtained at the standard telecommunication wavelength of 1550 nm . Note that r is in general wavelength-dependent and usually increases towards smaller wavelengths. The first class of EO modulators is based on crystalline materials, for which the implementation on well-established photonic platforms such as Si photonics was considered challenging and cumbersome. Recently, however, thin films of LiNbO_3 were fabricated and bonded to various substrates such as SOI wafers [17]. In this approach, the EO properties of bulk LiNbO_3 can be maintained, leading to devices with EO coefficients of $r_{33} = 31 \text{ pm}/\text{V}$ [37]. Much higher effective EO coefficients of $r_{\text{eff}} = 300 \text{ pm}/\text{V}$ are realized on the hybrid BaTiO_3 -on-SOI platform [18]. Here, the crystalline BaTiO_3 is grown by a sophisticated molecular beam epitaxy process, which complicates implementation of efficient phase shifter structures. Much simpler processing is achieved with OEO materials, which additionally open the possibility of theory-guided molecular design for tailoring the optical properties. All-polymer EO waveguides reach $r_{33} = 86 \text{ pm}/\text{V}$ [8], whereas $r_{33} = 215 \text{ pm}/\text{V}$ was demonstrated in TiO_2 slot waveguides infiltrated with the commercial OEO material SEO100 [47]. Slightly higher in-device EO coefficients of $r_{33} = 220 \text{ pm}/\text{V}$ were realized in POH modulators employing a binary chromophore compound (BCC) [23]. The highest value for an SOH modulator so far was achieved with the binary chromophore organic glass (BCOG) PSLD41/YLD124 and amounts to $r_{33} = 230 \text{ pm}/\text{V}$ [25]. The SOH modulator presented in this work features a record-high in-device coefficient of $r_{33} = 390 \text{ pm}/\text{V}$. In general, the EO coefficient can be further increased when the operating wavelength approaches the absorption maximum of the employed EO material. For example, for the POH modulator discussed in [23], the absorption of the OEO material peaks at a wavelength around 900 nm , and an increased EO coefficient of $325 \text{ pm}/\text{V}$ is found at a wavelength of 1250 nm . Operating the presented SOH device at this wavelength may hence lead to even higher EO coefficients, potentially exceeding even $600 \text{ pm}/\text{V}$.

Data transmission experiment

To demonstrate the viability of the SOH MZM for high-speed data transmission, we generate on-off-keying (OOK) signals at data rates of 40 Gbit/s. The experimental setup is shown in Fig. 4(a). A pseudo random bit sequence of length $2^{15}-1$ at 40 Gbit/s is obtained from an arbitrary waveform generator (AWG) and applied to the device by a microwave probe without further amplification. The MZM is biased at its quadrature point and terminated by an external $50\ \Omega$ impedance in order to reduce reflections of the RF field.

An erbium-doped fiber amplifier (EDFA) after the MZM amplifies the optical signal to a constant power of 8 dBm. A 0.6 nm band pass filter (BP) is used to suppress the amplified spontaneous emission noise of the EDFA. The optical signal is then detected by a high-speed photodiode and a real-time oscilloscope. To increase the bandwidth of the SOH modulator we decrease the resistance of the doped silicon slabs by applying a gate field [31] of 0.18 V/nm, see Fig. 2 (b). We equalize the detected signal, thereby compensating the frequency response of the entire signal path including AWG, oscilloscope and the SOH modulator. The total fiber coupling losses amount to 8.9 dB, and the optical on-chip insertion loss of the MZM adds another 8.2 dB. The on-chip losses are caused by non-ideal MMI-couplers, lossy Si strip waveguides and strip-to-slot converters. The Si slot waveguide losses amount to about 3.9 dB/mm and are mainly attributed to the sidewall roughness of the slot. It can hence be assumed that more advanced lithography processes will allow to further reduce these losses in the future. In fact, it has been already shown that asymmetric strip-loaded Si slot waveguides with propagation losses as low as 0.2 dB/mm can be realized [48].

The device used for the data transmission experiment features a U_{π} of 270 mV. Fig. 4(b) shows the recorded eye diagram for a peak-to-peak drive voltage of only 140 mV_{pp}. We did not observe any errors in our 130 μ s-long recording containing roughly 5×10^6 symbols. For that reason, we rely on the Q factor of the eye diagram to estimate the bit error ratio (BER), assuming that the signal does not feature any intersymbol interference (ISI) and is impaired by additive white Gaussian noise only. For the 140 mV_{pp}-operation, we obtain a measured Q factor of 7.35, which leads to an estimated BER of approximately 1×10^{-13} . This is well below the 1×10^{-9} limit for error-free transmission. To the best of our knowledge, this is the smallest drive voltage for error-free OOK signaling at 40 Gbit/s reported so far. The energy consumption amounts to 2.5 fJ per bit and is mainly caused by the power dissipation in the $50\ \Omega$ termination of the device. Operating the devices as a purely capacitive load as in [19] could further reduce the energy consumption. Since the drive voltage is well below the actual U_{π} of the device (270 mV), the signal quality can be further improved by increasing the drive voltage. The eye diagram for a drive voltage of 260 mV_{pp} is depicted in Fig. 4(c) and shows an even wider eye opening. The measured Q factor amounts to 9.10.

Summary and Outlook

We demonstrate a silicon-organic hybrid (SOH) Mach-Zehnder modulator (MZM) featuring a record-high in-device electro-optic (EO) coefficient of $r_{33} = 390\ \text{pm/V}$ by employing the highly efficient EO chromophore JRD1. This is the highest material-related value for an in-device EO coefficient ever published for any material platform. The reported r_{33} is almost a factor of two larger compared to previously published values for SOH or plasmonic-organic hybrid (POH) modulators operating at the same wavelength of 1550 nm [20,25]. The devices feature ultra-small voltage-length products down to $U_{\pi}L = 0.32\ \text{Vmm}$ along with loss-efficiency products of $aU_{\pi}L = 1.2\ \text{VdB}$. Devices as short as 320 μm may hence be directly driven from binary

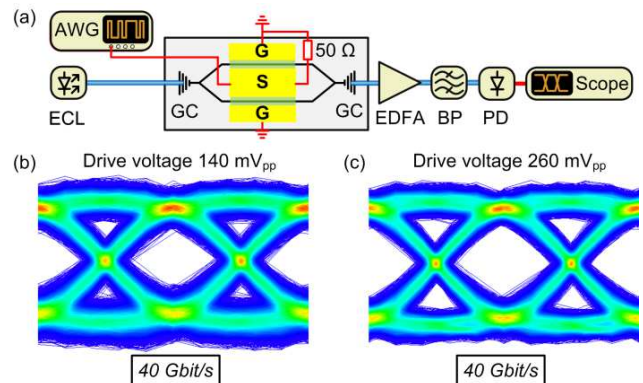


Fig. 4 Data transmission experiments. **(a)** Schematic of the experimental setup. Signals obtained from an arbitrary waveform generator (AWG) are fed to the MZM via microwave probes. The optical carrier provided by an external-cavity laser (ECL) is coupled to and from the chip by grating couplers (GC). The modulated light is amplified by an erbium doped fiber amplifier (EDFA), filtered using a band pass filter (BP), and detected by a high-speed photodiode (PD) connected to a real-time oscilloscope for recording eye diagrams. **(b)** Measured eye diagram at 40 Gbit/s for a drive voltage of 140 mV_{pp}. The bit error ratio (BER) is estimated from the measured Q factor of 7.35 and amounts to approximately $1 \cdot 10^{-13}$. This is well below the 10^{-9} limit for error-free transmission. **(c)** Measured eye diagram at 40 Gbit/s for a drive voltage of 260 mV_{pp}. The measured Q factor amounts to 9.10. The improved signal quality in comparison to (b) is caused by the fact that the drive voltage approaches the π -voltage of the device ($U_{\pi} = 270\ \text{mV}$) resulting in a wider eye opening. Post-equalization was applied to both received signals.

outputs of energy-efficient CMOS electronics [41], providing voltage swings of the order of 1 V. For these devices, optical propagation losses in the phase shifter sections would amount to less than 1.5 dB, leading to total insertion losses of less than 2 dB when assuming existing implementations of strip-to-slot mode converters [49] and MMI couplers [50] without any further optimization. This compares favorably to competing device concepts such as silicon-based depletion-type pn modulators [51,52] or POH devices [20]. The viability of the presented modulator is demonstrated by generating OOK signals at a data rate of 40 Gbit/s. We find that error-free transmission is achieved for a record-low drive voltage of only 140 mV_{pp}.

Funding. The European Research Council (ERC Starting Grant ‘EnTeraPIC’, # 280145), the EU FP7 projects PhoxTroT and BigPipes, the Alfred Krupp von Bohlen und Halbach Foundation, the Helmholtz International Research School for Teratronics (HIRST), the Karlsruhe School of Optics and Photonics (KSOP), the Karlsruhe Nano-Micro Facility (KNMF), the National Science Foundation (DMR-1303080) and the Air Force Office of Scientific Research (FA9550-15-1-0319).

Acknowledgment. The authors thank Bruce H. Robinson, Andreas Tillack, and Lewis E. Johnson for helpful discussions.

See [Supplement 1](#) for supporting content.

REFERENCES

1. I. P. Kaminow, T. Li, and A. E. Willner, *Optical Fiber Telecommunications V B : Systems and Networks* (Elsevier Academic Press, 2013).
2. A. Khilo, S. J. Spector, M. E. Grein, A. H. Nejadmalayeri, C. W. Holzwarth,

- M. Y. Sander, M. S. Dahlem, M. Y. Peng, M. W. Geis, N. A. DiLello, J. U. Yoon, A. Motamedi, J. S. Orcutt, J. P. Wang, C. M. Sorace-Agaskar, M. A. Popović, J. Sun, G.-R. Zhou, H. Byun, J. Chen, J. L. Hoyt, H. I. Smith, R. J. Ram, M. Perrott, T. M. Lyszczarz, E. P. Ippen, and F. X. Kärtner, "Photonic ADC: overcoming the bottleneck of electronic jitter," *Opt. Express* 20, 4454 (2012).
3. M. Laueremann, C. Weimann, A. Knopf, W. Heni, R. Palmer, S. Koeber, D. L. Elder, W. Bogaerts, J. Leuthold, L. R. Dalton, C. Rembe, W. Freude, and C. Koos, "Integrated optical frequency shifter in silicon-organic hybrid (SOH) technology," *Opt. Express* 24, 11694 (2016).
 4. G. Raybon, J. Cho, A. Adamiecki, P. Winzer, A. Konczykowska, F. Jorge, J.-Y. Dupuy, M. Riet, B. Duval, K. Kim, S. Randel, D. Pileri, B. Guan, N. K. Fontaine, and E. Burrows, "Single Carrier High Symbol Rate Transmitter for Data Rates up to 1.0 Tb/s," in *Optical Fiber Communication Conference (OSA)*, 2016, p. Th3A.2.
 5. S. Wolf, H. Zwickel, C. Kieninger, Y. Kutuvantavida, M. Laueremann, J. Lutz, L. Altenhain, R. Schmid, W. Freude, C. Koos, and S. Randel, "Silicon-Organic Hybrid (SOH) IQ Modulator for 100 GbD 16QAM Operation," in *Optical Fiber Communication Conference Postdeadline Papers (OSA)*, 2017, p. Th5C.1.
 6. C. Haffner, W. Heni, Y. Fedoryshyn, B. Baeuerle, A. Josten, Y. Salamin, R. Bonjour, C. Hoessbacher, A. Emboras, D. L. Elder, P. Leuchtmann, D. Hillerkuss, L. R. Dalton, C. Hafner, and J. Leuthold, "Ultra-compact plasmonic IQ-modulator," in *2015 European Conference on Optical Communication (ECOC) (IEEE)*, 2015, pp. 1–3.
 7. E. L. Wooten, K. M. Kissa, A. Yi-Yan, E. J. Murphy, D. A. Lafaw, P. F. Hallemeier, D. Maack, D. V. Attanasio, D. J. Fritz, G. J. McBrien, and D. E. Bossi, "A review of lithium niobate modulators for fiber-optic communications systems," *IEEE J. Sel. Top. Quantum Electron.* 6, 69–82 (2000).
 8. V. Katopodis, P. Groumas, Z. Zhang, R. Dinu, E. Miller, A. Konczykowska, J.-Y. Dupuy, A. Beretta, A. Dede, J. H. Choi, P. Harati, F. Jorge, V. Nodjadjim, M. Riet, G. Cangini, A. Vannucci, N. Keil, H.-G. Bach, N. Grote, H. Avramopoulos, and C. Kouloumentas, "Polymer enabled 100Gbaud connectivity for datacom applications," *Opt. Commun.* 362, 13–21 (2016).
 9. P. C. Schindler, D. Korn, C. Stamatidis, M. F. O'Keefe, L. Stampoulidis, R. Schmogrow, P. Zakynthinos, R. Palmer, N. Cameron, Y. Zhou, R. G. Walker, E. Kehayas, S. Ben-Ezra, I. Tomkos, L. Zimmermann, K. Petermann, W. Freude, C. Koos, and J. Leuthold, "Monolithic GaAs Electro-Optic IQ Modulator Demonstrated at 150 Gbit/s With 64QAM," *J. Light. Technol.* 32, 760–765 (2014).
 10. Y. Ogiso, J. Ozaki, Y. Ueda, N. Kashio, N. Kikuchi, E. Yamada, H. Tanobe, S. Kanazawa, H. Yamazaki, Y. Ohiso, T. Fujii, and M. Kohtoku, "Over 67 GHz Bandwidth and 1.5 V $\sqrt{\text{tr}}$ InP-Based Optical IQ Modulator With n-i-p-n Heterostructure," *J. Light. Technol.* 35, 1450–1455 (2017).
 11. C. Koos, J. Brosi, M. Waldow, W. Freude, and J. Leuthold, "Silicon-on-insulator modulators for next-generation 100 Gbit/s-Ethernet," in *33rd European Conference and Exhibition on Optical Communication - ECOC 2007 (IEE)*, 2007, Vol. 2007, pp. P056–P056.
 12. R. Ding, T. Baehr-Jones, Y. Liu, R. Bojko, J. Witzens, S. Huang, J. Luo, S. Benight, P. Sullivan, J.-M. Fedeli, M. Fournier, L. Dalton, A. Jen, and M. Hochberg, "Demonstration of a low $\sqrt{\text{tr}}$ L modulator with GHz bandwidth based on electro-optic polymer-clad silicon slot waveguides," *Opt. Express* 18, 15618–23 (2010).
 13. C. Koos, J. Leuthold, W. Freude, M. Kohl, L. Dalton, W. Bogaerts, A. L. Giesecke, M. Laueremann, A. Melikyan, S. Koeber, S. Wolf, C. Weimann, S. Muehlbrandt, K. Koehnle, J. Pfeifle, W. Hartmann, Y. Kutuvantavida, S. Ummethala, R. Palmer, D. Korn, L. Alloatti, P. C. Schindler, D. L. Elder, T. Wahlbrink, and J. Bolten, "Silicon-Organic Hybrid (SOH) and Plasmonic-Organic Hybrid (POH) Integration," *J. Light. Technol.* 34, 256–268 (2016).
 14. A. Melikyan, L. Alloatti, A. Muslija, D. Hillerkuss, P. C. Schindler, J. Li, R. Palmer, D. Korn, S. Muehlbrandt, D. Van Thourhout, B. Chen, R. Dinu, M. Sommer, C. Koos, M. Kohl, W. Freude, and J. Leuthold, "High-speed plasmonic phase modulators," *Nat. Photonics* 8, 229–233 (2014).
 15. C. Haffner, W. Heni, Y. Fedoryshyn, J. Niegemann, A. Melikyan, D. L. Elder, B. Baeuerle, Y. Salamin, A. Josten, U. Koch, C. Hoessbacher, F. Ducry, L. Juchli, A. Emboras, D. Hillerkuss, M. Kohl, L. R. Dalton, C. Hafner, and J. Leuthold, "All-plasmonic Mach-Zehnder modulator enabling optical high-speed communication at the microscale," *Nat. Photonics* 9, 525–528 (2015).
 16. A. Melikyan, K. Koehnle, M. Laueremann, R. Palmer, S. Koeber, S. Muehlbrandt, P. C. Schindler, D. L. Elder, S. Wolf, W. Heni, C. Haffner, Y. Fedoryshyn, D. Hillerkuss, M. Sommer, L. R. Dalton, D. Van Thourhout, W. Freude, M. Kohl, J. Leuthold, and C. Koos, "Plasmonic-organic hybrid (POH) modulators for OOK and BPSK signaling at 40 Gbit/s," *Opt. Express* 23, 9938 (2015).
 17. P. O. Weigel, M. Savanier, C. T. DeRose, A. T. Pomerene, A. L. Starbuck, A. L. Lentine, V. Stenger, and S. Mookherjee, "Lightwave Circuits in Lithium Niobate through Hybrid Waveguides with Silicon Photonics," *Sci. Rep.* 6, 22301 (2016).
 18. S. Abel, T. Stöferle, C. Marchiori, D. Caimi, L. Czornomaz, M. Stuckelberger, M. Sousa, B. J. Offrein, and J. Fompeyrine, "A Hybrid Barium Titanate-Silicon Photonics Platform for Ultraefficient Electro-Optic Tuning," *J. Light. Technol.* 34, (2016).
 19. S. Koeber, R. Palmer, M. Laueremann, W. Heni, D. L. Elder, D. Korn, M. Woessner, L. Alloatti, S. Koenig, P. C. Schindler, H. Yu, W. Bogaerts, L. R. Dalton, W. Freude, J. Leuthold, and C. Koos, "Femtojoule electro-optic modulation using a silicon-organic hybrid device," *Light Sci. Appl.* 4, e255 (2015).
 20. W. Heni, C. Haffner, D. L. Elder, A. F. Tillack, Y. Fedoryshyn, R. Cottier, Y. Salamin, C. Hoessbacher, U. Koch, B. Cheng, B. Robinson, L. R. Dalton, and J. Leuthold, "Nonlinearities of organic electro-optic materials in nanoscale slots and implications for the optimum modulator design," *Opt. Express* 25, 2627 (2017).
 21. C. Hoessbacher, A. Josten, B. Baeuerle, Y. Fedoryshyn, H. Hettrich, Y. Salamin, W. Heni, C. Haffner, C. Kaiser, R. Schmid, D. L. Elder, D. Hillerkuss, M. Möller, L. R. Dalton, and J. Leuthold, "Plasmonic modulator with >170 GHz bandwidth demonstrated at 100 GbD NRZ," *Opt. Express* 25, 1762 (2017).
 22. R. W. Boyd, *Nonlinear Optics* (Academic Press, 2008).
 23. C. Haffner, W. Heni, D. L. Elder, Y. Fedoryshyn, N. Đorđević, D. Chelladurai, U. Koch, K. Portner, M. Burla, B. Robinson, L. R. Dalton, and J. Leuthold, "Harnessing nonlinearities near material absorption resonances for reducing losses in plasmonic modulators," *Opt. Mater. Express* 7, 2168 (2017).
 24. W. Jin, P. V. Johnston, D. L. Elder, A. F. Tillack, B. C. Olbricht, J. Song, P. J. Reid, R. Xu, B. H. Robinson, and L. R. Dalton, "Benzocyclobutene barrier layer for suppressing conductance in nonlinear optical devices during electric field poling," *Appl. Phys. Lett.* 104, 243304 (2014).
 25. R. Palmer, S. Koeber, D. L. Elder, M. Woessner, W. Heni, D. Korn, M. Laueremann, W. Bogaerts, L. Dalton, W. Freude, J. Leuthold, and C. Koos, "High-Speed, Low Drive-Voltage Silicon-Organic Hybrid Modulator Based on a Binary-Chromophore Electro-Optic Material," *J. Light. Technol.* 32, 2726–2734 (2014).
 26. A. F. Tillack and B. H. Robinson, "Toward optimal EO response from ONLO chromophores: a statistical mechanics study of optimizing shape," *J. Opt. Soc. Am. B* 33, E121 (2016).
 27. W. Heni, Y. Kutuvantavida, C. Haffner, H. Zwickel, C. Kieninger, S. Wolf, M. Laueremann, Y. Fedoryshyn, A. F. Tillack, L. E. Johnson, D. L. Elder, B. H. Robinson, W. Freude, C. Koos, J. Leuthold, and L. R. Dalton, "Silicon-Organic and Plasmonic-Organic Hybrid Photonics," *ACS Photonics* 4, 1576–1590 (2017).
 28. W. Jin, P. V. Johnston, D. L. Elder, K. T. Manner, K. E. Garrett, W. Kaminsky, R. Xu, B. H. Robinson, and L. R. Dalton, "Structure-function relationship exploration for enhanced thermal stability and electro-optic activity in monolithic organic NLO chromophores," *J. Mater. Chem. C* 4, 3119–3124 (2016).
 29. J. Luo, S. Huang, Z. Shi, B. M. Polishak, X.-H. Zhou, and A. K. Jen, "Tailored Organic Electro-optic Materials and Their Hybrid Systems for Device Applications †," *Chem. Mater.* 23, 544–553 (2011).
 30. L. R. Dalton, P. A. Sullivan, and D. H. Bale, "Electric Field Poled Organic Electro-optic Materials: State of the Art and Future Prospects," *Chem. Rev.* 110, 25–55 (2010).
 31. L. Alloatti, R. Palmer, S. Diebold, K. P. Pahl, B. Chen, R. Dinu, M. Fournier, J.-M. Fedeli, T. Zwick, W. Freude, C. Koos, and J. Leuthold, "100

- GHz silicon-organic hybrid modulator," *Light Sci Appl* 3, e173 (2014).
32. L. R. Dalton, D. Lao, B. C. Olbricht, S. Benight, D. H. Bale, J. A. Davies, T. Ewy, S. R. Hammond, and P. A. Sullivan, "Theory-inspired development of new nonlinear optical materials and their integration into silicon photonic circuits and devices," *Opt. Mater. (Amst)*. 32, 658–668 (2010).
 33. M. Sprave, R. Blum, and M. Eich, "High electric field conduction mechanisms in electrode poling of electro-optic polymers," *Appl. Phys. Lett.* 69, 2962–2964 (1996).
 34. S. Huang, T.-D. Kim, J. Luo, S. K. Hau, Z. Shi, X.-H. Zhou, H.-L. Yip, and A. K.-Y. Jen, "Highly efficient electro-optic polymers through improved poling using a thin TiO₂-modified transparent electrode," *Appl. Phys. Lett.* 96, 243311 (2010).
 35. T. Hiraki, T. Aihara, K. Hasebe, K. Takeda, T. Fujii, T. Kakitsuka, T. Tsuchizawa, H. Fukuda, and S. Matsuo, "Heterogeneously integrated III–V/Si MOS capacitor Mach-Zehnder modulator," *Nat. Photonics* 11, 482–485 (2017).
 36. J.-H. Han, F. Boeuf, J. Fujikata, S. Takahashi, S. Takagi, and M. Takenaka, "Efficient low-loss InGaAsP/Si hybrid MOS optical modulator," *Nat. Photonics* 11, 486–490 (2017).
 37. A. Rao, A. Patil, J. Chiles, M. Malinowski, S. Novak, K. Richardson, P. Rabiei, and S. Fathpour, "Heterogeneous microring and Mach-Zehnder modulators based on lithium niobate and chalcogenide glasses on silicon," *Opt. Express* 23, 22746 (2015).
 38. C. Xiong, W. H. P. Pernice, J. H. Ngai, J. W. Reiner, D. Kumah, F. J. Walker, C. H. Ahn, and H. X. Tang, "Active Silicon Integrated Nanophotonics: Ferroelectric BaTiO₃ Devices," *Nano Lett.* 14, 1419–1425 (2014).
 39. F. Eltes, D. Caimi, F. Fallegger, M. Sousa, E. O'Connor, M. D. Rossell, B. Offrein, J. Fompeyrine, and S. Abel, "Low-Loss BaTiO₃-Si Waveguides for Nonlinear Integrated Photonics," *ACS Photonics* 3, 1698–1703 (2016).
 40. Z. Yong, W. D. Sacher, Y. Huang, J. C. Mikkelsen, Y. Yang, X. Luo, P. Dumais, D. Goodwill, H. Bahrami, G.-Q. Lo, E. Bernier, and J. K. Poon, "Efficient Single-Drive Push-Pull Silicon Mach-Zehnder Modulators with U-Shaped PN Junctions for the O-Band," in *Optical Fiber Communication Conference (OSA, 2017)*, p. Tu2H.2.
 41. S. Wolf, M. Lauermann, P. Schindler, G. Ronniger, K. Geistert, R. Palmer, S. Kober, W. Bogaerts, J. Leuthold, W. Freude, and C. Koos, "DAC-Less Amplifier-Less Generation and Transmission of QAM Signals Using Sub-Volt Silicon-Organic Hybrid Modulators," *J. Light. Technol.* 33, 1425–1432 (2015).
 42. M. Lauermann, R. Palmer, S. Koeber, P. C. Schindler, D. Korn, T. Wahlbrink, J. Bolten, M. Waldow, D. L. Elder, L. R. Dalton, J. Leuthold, W. Freude, and C. Koos, "Low-power silicon-organic hybrid (SOH) modulators for advanced modulation formats," *Opt. Express* 22, 29927 (2014).
 43. M. Lauermann, S. Wolf, P. C. Schindler, R. Palmer, S. Koeber, D. Korn, L. Alloatti, T. Wahlbrink, J. Bolten, M. Waldow, M. Koenigsmann, M. Kohler, D. Malsam, D. L. Elder, P. V. Johnston, N. Phillips-Sylvain, P. A. Sullivan, L. R. Dalton, J. Leuthold, W. Freude, and C. Koos, "40 GBd 16QAM Signaling at 160 Gb/s in a Silicon-Organic Hybrid Modulator," *J. Light. Technol.* 33, 1210–1216 (2015).
 44. H. Zwickel, S. Wolf, C. Kieninger, Y. Kutuvantavida, M. Lauermann, T. De Keulenaer, A. Vyncke, R. Vaernewyck, J. Luo, A. K.-Y. Jen, W. Freude, J. Bauwelinck, S. Randel, and C. Koos, "Silicon-organic hybrid (SOH) modulators for intensity-modulation / direct-detection links with line rates of up to 120 Gbit/s," *Opt. Express*, accepted (2017).
 45. S. Wolf, H. Zwickel, W. Hartmann, M. Lauermann, Y. Kutuvantavida, C. Kieninger, L. Altenhain, R. Schmid, J. Luo, A. K.-Y. Jen, S. Randel, W. Freude, and C. Koos, "Silicon-Organic Hybrid (SOH) Mach-Zehnder Modulators for 100 Gbit/s On-Off Keying," arXiv:1709.01793 [physics.app-ph] (2017).
 46. X. Wang, C.-Y. Lin, S. Chakravarty, J. Luo, A. K.-Y. Jen, and R. T. Chen, "Effective in-device r₃₃ of 735 pm/V on electro-optic polymer infiltrated silicon photonic crystal slot waveguides," *Opt. Lett.* 36, 882 (2011).
 47. Y. Enami, H. Nakamura, J. Luo, and A. K.-Y. Jen, "Analysis of efficiently poled electro-optic polymer/TiO₂ vertical slot waveguide modulators," *Opt. Commun.* 362, 77–80 (2016).
 48. R. Ding, T. Baehr-Jones, W.-J. Kim, B. Boyko, R. Bojko, A. Spott, A. Pomerene, C. Hill, W. Reinhardt, and M. Hochberg, "Low-loss asymmetric strip-loaded slot waveguides in silicon-on-insulator," *Appl. Phys. Lett.* 98, 233303 (2011).
 49. R. Palmer, L. Alloatti, D. Korn, W. Heni, P. C. Schindler, J. Bolten, M. Karl, M. Waldow, T. Wahlbrink, W. Freude, C. Koos, and J. Leuthold, "Low-Loss Silicon Strip-to-Slot Mode Converters," *IEEE Photonics J.* 5, 2200409–2200409 (2013).
 50. Zhen Sheng, Zhiqi Wang, Chao Qiu, Le Li, A. Pang, Aimin Wu, Xi Wang, Shichang Zou, and Fuwan Gan, "A Compact and Low-Loss MMI Coupler Fabricated With CMOS Technology," *IEEE Photonics J.* 4, 2272–2277 (2012).
 51. C. Xiong, D. M. Gill, J. E. Proesel, J. S. Orcutt, W. Haensch, and W. M. J. Green, "Monolithic 56 Gb/s silicon photonic pulse-amplitude modulation transmitter," *Optica* 3, 1060 (2016).
 52. D. Patel, A. Samani, V. Veerasubramanian, S. Ghosh, and D. V. Plant, "Silicon Photonic Segmented Modulator-Based Electro-Optic DAC for 100 Gb/s PAM-4 Generation," *IEEE Photonics Technol. Lett.* 27, 2433–2436 (2015).

Ultra-High In-Device Electro-Optic Coefficient of $r_{33} = 390$ pm/V Demonstrated in a Silicon-Organic Hybrid (SOH) Modulator

CLEMENS KIENINGER,^{1,2,*} YASAR KUTUVANTAVIDA,^{1,2} DELWIN L. ELDER,³ STEFAN WOLF,¹ HEINER ZWICKEL,¹ MATTHIAS BLAICHER,¹ JUNED N. KEMAL,¹ MATTHIAS LAUERMANN,⁴ SEBASTIAN RANDEL,¹ WOLFGANG FREUDE,¹ LARRY R. DALTON,³ AND CHRISTIAN KOOS^{1,2,*}

¹Karlsruhe Institute of Technology (KIT), Institute of Photonics and Quantum Electronics (IPQ), Karlsruhe 76131, Germany

²Karlsruhe Institute of Technology (KIT), Institute of Microstructure Technology (IMT), Karlsruhe 76344, Germany

³University of Washington, Department of Chemistry, Seattle, WA 98195, USA

⁴Now with: Infinera Corporation, Sunnyvale, CA 94089, USA

*Corresponding authors: clemens.kieninger@kit.edu, christian.koos@kit.edu

This document provides supplementary information to “Ultra-High In-Device Electro-Optic Coefficient of $r_{33} = 390$ pm/V Demonstrated in a Silicon-Organic Hybrid (SOH) Modulator,”. In the first part, the experimental setup for the π -voltage measurement of the SOH modulator is described. The second part includes a more detailed discussion of the on-chip losses of the modulator. The third part gives the mathematical relations that are used to link the measured U_{π} to the in-device EO coefficient r_{33} of the SOH modulator.

Experimental Setup for the π -voltage measurement

The experimental setup for the measurement of the π -voltage U_{π} of the silicon-organic hybrid (SOH) modulator is depicted in Fig. S1.

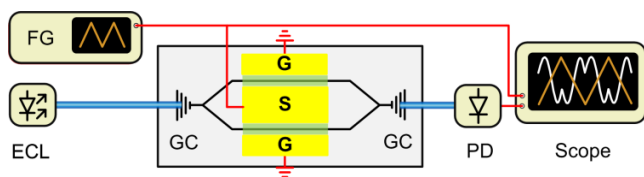


Fig.S1 Experimental setup for the π -voltage measurement. A triangular waveform obtained from a function generator (FG) is fed to the SOH modulator while an optical carrier obtained from an external cavity laser (ECL) is coupled to and from the chip via grating couplers (GC). The over-modulated optical signal is detected with a photodiode and an oscilloscope which also monitors the output of the FG. U_{π} can be read out as the voltage increment needed to drive the modulator from minimum to maximum transmission.

The optical carrier obtained from an external cavity laser (ECL) is coupled to and from the silicon photonics chip via grating couplers (GC) while a triangular waveform obtained from a function generator (FG) is fed to the SOH Mach-Zehnder Modulator (MZM) via microwave probes. The modulated light is detected with a photodiode that is connected to an oscilloscope. The oscilloscope monitors additionally the drive voltage applied to the MZM. The modulator is biased in its 3 dB point and the amplitude of the triangular waveform is chosen such that the modulator is over-modulated, that is, the peak-to-peak drive voltage is larger than the U_{π} of the device under test. In this case, U_{π} can be directly read out on the oscilloscope as the voltage increment needed to drive the modulator from its minimum to its maximum transmission point, see Fig. 2(c) and (d) of the main text.

Optical loss of the SOH modulator

The total fiber-to-chip coupling losses amount to 8.9 dB caused by the non-ideal grating couplers. The on-chip loss of the MZM amounts to 8.2 dB. These on-chip losses can be decomposed into

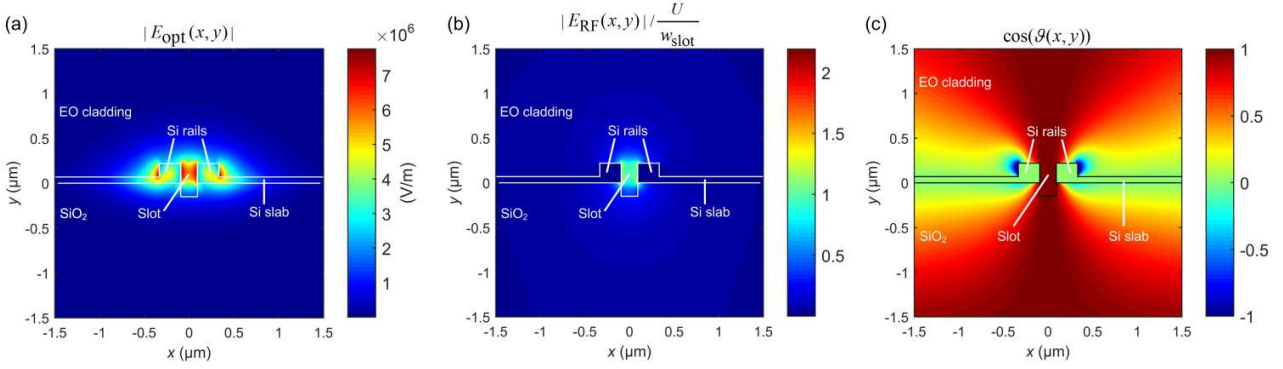


Fig. S2 Simulation results. (a) Magnitude of the optical field $|E_{\text{opt}}(x, y)|$ for a launched optical power of 20 mW. (b) Normalized magnitude of the RF field, $|E_{\text{RF}}(x, y)| / \frac{U}{w_{\text{slot}}}$ which amounts to about unity in the center of the slot, due to the normalization. Both optical and RF mode are tightly confined to the EO-material-filled slot region which results in efficient modulation. (c) $\cos(\vartheta(x, y))$, where $\vartheta(x, y)$ is the angle between field lines of the optical and the RF mode. In, as well as above and below the slot region, field lines of optical and RF field are parallel resulting in $\cos(\vartheta(x, y)) = 1$. Directly above the slabs $\cos(\vartheta(x, y))$ amounts to zero since the field lines are perpendicular. For all simulations we assume that the slot is over-etched by 150 nm.

passive components and the loss in the SOH slot waveguide. The passive components include two multi-mode interference (MMI) couplers with losses of 0.37 dB per coupler, two optical mode converters at the strip-slot waveguide interfaces with losses of 0.20 dB per converter, and strip-waveguide propagation losses of 1.3 dB. The remaining 5.8 dB are attributed to the SOH slot waveguide propagation losses of the 1.5 mm long MZM which results in a propagation loss of 3.9 dB/mm. This includes both scattering loss from the slot waveguide sidewalls and free-carrier absorption loss in the doped silicon waveguide structures. Note that dedicated test structures were used to determine the grating coupler losses and the losses of the MMI couplers and the mode converter structures. The propagation losses of the strip waveguide amount to 2.5 dB/cm, specified by the chip manufacturer.

Mathematical relations for calculating the in-device r_{33} of the SOH MZM

The phase change $\Delta\varphi$ of the optical carrier in the silicon-organic hybrid (SOH) modulator can be written as [1]

$$\Delta\varphi = n_{\text{EO}}^4 \frac{\epsilon_0 c \pi L}{2 \lambda P} \times \int_{-\infty}^{\infty} \int_{-\infty}^{\infty} r_{33}(x, y) E_{\text{RF,EO}}(x, y) |E_{\text{opt,EO}}(x, y)|^2 dx dy, \quad (\text{S1})$$

where n_{EO} is the refractive index of the organic electro-optic (EO) material, ϵ_0 is the vacuum permittivity, c is the vacuum speed of light, L is the length of the modulator, λ is the wavelength of the optical carrier, $r_{33}(x, y)$ is the non-uniform EO coefficient. $E_{\text{RF,EO}}(x, y)$ is the component of the vectorial mode field of the applied radio frequency (RF) field pointing in the direction of the local chromophore orientation, which is defined by the axis of the molecular dipole. Similarly, $E_{\text{opt,EO}}(x, y)$ is the corresponding component of the vectorial mode field of the optical carrier. The parameter P is the power of the optical mode, which is defined as

$$P = \frac{1}{2} \int_{-\infty}^{\infty} \int_{-\infty}^{\infty} \text{Re}\{\mathbf{E}_{\text{opt}}(x, y) \times \mathbf{H}_{\text{opt}}^*(x, y)\} \cdot \hat{\mathbf{z}} dx dy. \quad (\text{S2})$$

The non-uniformity of $r_{33}(x, y)$ is caused by the inhomogeneity of the electric poling field that dictates the local orientation of the

chromophore dipoles. Due to this non-uniformity we report here on the mean value of the EO coefficient $\overline{r_{33}}_{\text{slot}}$ in the slot region of the SOH modulator, i.e., the region between the Si rails. We furthermore assume a linear dependence of r_{33} on the poling field E_{pol} and approximate the (x, y) -dependency of the static poling field by the (x, y) -dependency of the RF mode field. This leads to

$$r_{33}(x, y) = \overline{r_{33}}_{\text{slot}} \frac{|E_{\text{pol}}(x, y)|}{|E_{\text{pol}}|_{\text{slot}}} \rho(x, y) \approx \overline{r_{33}}_{\text{slot}} \frac{|E_{\text{RF}}(x, y)|}{|E_{\text{RF}}|_{\text{slot}}} \rho(x, y), \quad (\text{S3})$$

where $\overline{|E_{\text{pol}}|}_{\text{slot}}$ and $\overline{|E_{\text{RF}}|}_{\text{slot}}$ are the mean values of the magnitude of the static poling field and the RF field in the slot region, respectively and $\rho(x, y)$ is unity for (x, y) -values in the EO material and zero otherwise. By using Eq. (S3) we can rewrite Eq. (S1) as

$$\Delta\varphi = n_{\text{EO}}^4 \frac{\epsilon_0 c \pi L}{2 \lambda P} \overline{r_{33}}_{\text{slot}} \times \int_{-\infty}^{\infty} \int_{-\infty}^{\infty} \frac{|E_{\text{RF}}(x, y)|}{|E_{\text{RF}}|_{\text{slot}}} \rho(x, y) E_{\text{RF,EO}}(x, y) |E_{\text{opt,EO}}(x, y)|^2 dx dy. \quad (\text{S4})$$

Since the chromophore dipole moments align along the poling field (which is approximated by the RF field), the component $E_{\text{RF,EO}}(x, y)$ is simply given by the magnitude of the RF field $|E_{\text{RF}}(x, y)|$. For the corresponding component of the optical mode we can deduce $|E_{\text{opt,EO}}(x, y)| = |E_{\text{opt}}(x, y)| \cos(\vartheta(x, y))$, where $\vartheta(x, y)$ is the angle between field lines of the optical and the RF mode. Finally, we normalize the RF field by U/w_{slot} , where U is the RF voltage which is applied across the SOH slot waveguide and w_{slot} is the slot width. Using these simplifications the induced phase change writes

$$\Delta\varphi = n_{\text{EO}}^4 \frac{\epsilon_0 c \pi L}{2 \lambda P} \overline{r_{33}}_{\text{slot}} \frac{U}{w_{\text{slot}}} \times \int_{-\infty}^{\infty} \int_{-\infty}^{\infty} \frac{|E_{\text{RF}}(x, y)|^2 \rho(x, y)}{|E_{\text{RF}}|_{\text{slot}} U / w_{\text{slot}}} |E_{\text{opt}}(x, y)|^2 \cos^2(\vartheta(x, y)) dx dy. \quad (\text{S5})$$

The SOH modulator is implemented as a Mach-Zehnder modulator (MZM) with a ground-signal-ground (GSG) transmission line configuration realizing push-pull operation. Therefore, for a total

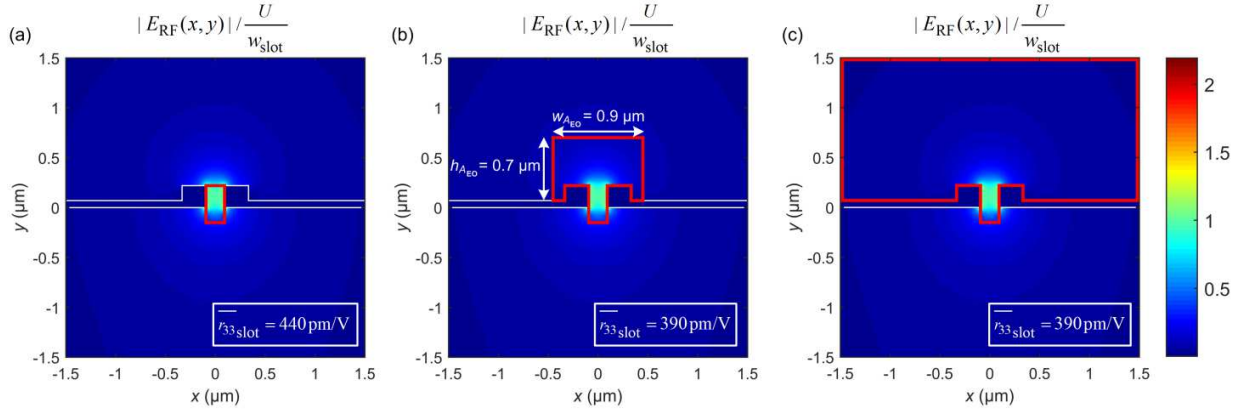


Fig. S3 Influence of choice of finite integration area A_{EO} on calculated $\overline{r}_{33\text{slot}}$. Depicted is the normalized magnitude of the RF field $|E_{RF}(x, y)| / \frac{U}{w_{\text{slot}}}$ and different integration areas A_{EO} are indicated by red lines. (a) The integration area A_{EO} includes only the slot region and the over-etched volume. The corresponding $\overline{r}_{33\text{slot}}$ would amount to 440 pm/V, which overestimates the actual value. (b) $\overline{r}_{33\text{slot}}$ decreases and converges to a constant value for growing A_{EO} . For an integration area width and height of $w_{AEO} = 0.9 \mu\text{m}$ and $h_{AEO} = 0.7 \mu\text{m}$, respectively, the limit of $\overline{r}_{33\text{slot}} = 390 \text{ pm/V}$ is reached. (c) Increasing the integration area over the whole displayed range doesn't decrease the calculated $\overline{r}_{33\text{slot}}$ any further.

phase shift of π , the phase is shifted by only $\pm\pi/2$ in the two arms of the MZM, respectively. As a consequence, the mean value of the EO coefficient in the slot region $\overline{r}_{33\text{slot}}$ is linked to the π -voltage U_π by

$$\overline{r}_{33\text{slot}} = \frac{\lambda w_{\text{slot}}}{2n_{EO}^3 U_\pi L} \times \left(\frac{\epsilon_0 c n_{EO}}{2P} \int_{-\infty}^{\infty} \int_{-\infty}^{\infty} \frac{|E_{RF}(x, y)|^2 \rho(x, y)}{|E_{RF}|_{\text{slot}} U / w_{\text{slot}}} |E_{\text{opt}}(x, y)|^2 \cos^2(\vartheta(x, y)) dx dy \right)^{-1} \quad (\text{S6})$$

The mode fields are simulated with the commercial software CST MICROWAVE STUDIO by using a finite integration method. The magnitude of the optical field for a launched power of 20 mW is depicted in Fig. S2(a). Fig. S2(b) shows the magnitude of the RF field at a frequency of 20 GHz normalized by U/w_{slot} . Since the electrical conductivity of the Si rails and slabs are much higher compared to the EO material and the lower SiO_2 cladding, these parts are modeled as perfect electric conductors. Due to the normalization, the plotted field amounts to approximately unity in the slot region. In close proximity to the corners of the rails, values of about 2 are reached, which is hardly visible in the figure. It can be seen that both the RF and the optical mode are tightly confined in the slot region, which results in highly efficient modulation of the SOH modulator concept. Simulation results for $\cos(\vartheta(x, y))$ are shown in Fig. S2(c). In the slot region as well as above and below the slot, field lines of RF and optical field are parallel resulting in $\cos(\vartheta(x, y)) \approx 1$ whereas further left and right of the slot $\cos(\vartheta(x, y))$ decreases and becomes zero directly above and below the silicon slabs. Near the outer sidewalls of the rails, values of $\cos(\vartheta(x, y)) \approx -1$ are found, since field lines of the optical and RF field are antiparallel in this region.

Note that the slot is slightly over-etched, generating a free volume underneath the slot, as indicated in Fig. S2. This was confirmed by cutting a trench perpendicular to the direction of propagation of the slot waveguide by using focused ion beam (FIB) milling and by subsequently investigating the cross section of the waveguide. We extracted an over-etch depth of $130 \pm 20 \text{ nm}$. For our simulations, we assume that the volume caused by the over-etching is entirely filled with the organic EO material, and for all simulations we use

an over-etch depth of 150 nm in order to not overestimate the calculated $\overline{r}_{33\text{slot}}$.

In praxis, the numerical evaluation of the integral in Eq. (S6) requires the limitation to a finite integration area A_{EO} rather than integration over the entire XY-plane. However, A_{EO} has to be carefully selected as $\overline{r}_{33\text{slot}}$ is overestimated if A_{EO} is chosen too small.

In Fig. S3, the normalized magnitude of the RF field $|E_{RF}(x, y)| / \frac{U}{w_{\text{slot}}}$ is depicted and three different integration areas A_{EO} are indicated by the red lines. In Fig. S3(a) A_{EO} extends only over the slot region and the over-etched region underneath the slot. Here, the calculated $\overline{r}_{33\text{slot}}$ would amount to 440 pm/V, which overestimates the actual value. This is due to the fact, that a considerable part of the RF and the optical mode are excluded from the chosen integration area A_{EO} . For growing integration area A_{EO} , $\overline{r}_{33\text{slot}}$ decreases and converges to a constant value of 390 pm/V. This value can be reached by only moderately extending A_{EO} with respect to the case shown in Fig. S3 (a), as illustrated in Fig. S3(b). Here, the integration area width and height amounts to $w_{AEO} = 0.9 \mu\text{m}$ and $h_{AEO} = 0.7 \mu\text{m}$, respectively. In Fig. S3(c) the integration area is extended over the whole displayed range. However, the corresponding $\overline{r}_{33\text{slot}} = 390 \text{ pm/V}$ does not change compared to the smaller integration area depicted in Fig. S3(b) since the contribution of the additionally included parts of the RF field and of the optical mode field is negligible.

References

1. C. Koos, *Nanophotonic Devices for Linear and Nonlinear Optical Signal Processing* (Univ.-Verl. Karlsruhe, 2007).